Radiation damage effects in space-borne CCD detectors

J. C. Terrazas Vargas [1,2]
Università Degli Studi di Torino (UNITO),
Via Giulia 1, *I*-10125 *Turin -ITALY*
terrazas@to.infn.it

L. Corcione[2], M. G. Lattanzi[2], and M. Gai[2]
Osservatorio Astronomico di Torino (OATo),
Via Osservatorio 20, *I*-10025 *Pino Torinese, Turin - ITALY*

ABSTRACT

This paper evaluates the astrometric and photometric implications of a series of laboratory tests conducted to study the effects of radiation damage caused by solar protons in space borne Charge Coupled Devices (CCDs). The photometric effects, i.e. charge loss (CL), and the astrometric effects, i.e. location biases, associated with the radiation-induced distortion on the sampled Line Spread Function(LSF), are assessed via a Gaussian fitting model. The data reduction is supported by a detailed analysis of the experimental set-up. Charge loss and centroid shift variations are evaluated as a function of the simulated star brightness and of the level of diffuse optical background, in order to derive useful hints for the modelling and calibration of the radiation damaged LSF during actual payload operations in orbit.

Subject headings: CCD: Radiation Damage, Line Spread Function (LSF), Charge Loss, Astrometric and Photometric effects, Charge Transfer Efficiency (CTE), Charge Transfer Inefficiency (CTI)

1. Introduction

The work presented in this article takes advantage of a laboratory experiment developed to study the properties of the imaging payload that is flying on the Gaia satellite since December 19, 2013, and that will be subjected, throughout its operational life time, to the environmental conditions of the region around the Lagrangian L2 point of the Sun-Earth system. For this reason we thought it useful to devote this introduction to the illustration of the most relevant traits of such a mission.

Gaia is a cornerstone mission of the European Space Agency (ESA), which uses a measurement schema similar to that of its predecessor Hipparcos (M. Perryman 2009) to build an extraordinary precise three-dimensional map of positions and motions of about one billion stars in our Galaxy. Gaia implements a 4 π sky survey from an orbit around the Lagrange point L2, at about 1.5 million km from Earth, by simultaneously imaging two fields of view, separated by a highly stable and large angle of 106.5° (the Basic Angle), onto the same focal plane made of a mosaic of 106 large format (4,500 x 1966 pixels) CCD detectors.

The focal plane assembly (FPA) is functionally split as follows: the Sky Mapper (SM) CCD's detect the objects entering the field of view and compute the position of subsequent readout windows; the Astrometric Field (AF) CCD's perform the exposures devoted to astrometric measurements; the Blue and Red Photometer CCD's provides spectro-photometric measurements at low resolution in the spectral range $330 - 680$ $[nm]$

[1]PhD Università Degli Studi di Torino (UNITO). Turin - Italy

[2]INAF-OATo; Osservatorio Astronomico di Torino (OATo), Turin - Italy

and $640 - 1000$ $[nm]$, respectively; the Radial Velocity Spectrometer provides moderate resolution spectra for objects brighter than $17th$ magnitude; Wave Front Sensors (WFS) and Basic-Angle Monitor (BAM) devices are used for initial instrument set-up and to monitor the evolution of key instrumental parameters along the mission. For more detailed and constantly updated information on the Gaia payload and on-board calibration subsystems the interested reader can consult the Gaia mission portal at: *http://www.esa.int/Our_Activities/Space_Science/Gaia*.

Since radiation damage on the detector was considered potentially critical, several test campaigns on the subject were performed to investigate the issue. Radiation test campaign CCN10. the laboratory experiment investigated in this article, was focused on the usage of *diffuse optical background* as a possible remedy to radiation damage.

2. Radiation environment

ESA's Gaia space mission is projected for 5 years operational lifetime, orbiting in the Lagrange 2 point (L2). Gaia operational environment is affected by a complex spectrum of natural space radiation, that includes solar wind plasma (95% protons, 5% He^{++}) and ionizing radiation (i.e. energetic electrons, ions, protons and alpha particles from solar flares / coronal mass ejections, Galactic cosmic rays and Jovian electrons). Some contributions are more or less continuous (cosmic rays), whereas others feature sudden peaks (solar flares).

Gaia works with one of the most complex CCD mosaics ever build, designed and manufactured by **e2v** technologies (UK). Each CCD in the Gaia Focal plane fulfills different Astrophysical functions such as Astrometry (parallaxes, Positions, proper motions), Photometry (magnitudes) Spectro-Photometry (Star temperatures, gravities, metallicity, etc) and Spectroscopy (Radial Velocities).

The radiation environment in which the CCD's will operate is a critical factor, which can seriously restrict Gaia performances. Concerning the effects on Gaia CCD's, the interplanetary environment in $L2$ can essentially be considered to be dominated by solar-flare protons (G.R. Hopkinson 1996), whose most critical damage to Gaia CCD's occurs in terms of non-ionizing or displacement damage, which is associated with the generation of electron traps as solar protons pass through the epitaxial silicon, collide with silicon atoms, and displace them from their locations in the crystal lattice.

Disruption of the crystal lattice introduces spurious energy levels in the semiconductor band gap, which are responsible for photo-electron trapping and de-trapping. Because of the CCD TDI readout mode, there are statistical processes of electron capture and release, which occur with different time constants, depending on the trap species, and drastically affect all the Gaia photometric, astrometric and spectroscopic measurements with photometric and astrometric errors due to charge loss and the deformation of the image profile. The (minimal) shielding offered by the large Gaia focal plane assembly (FPA) reduces the non-ionizing (displacement-damage) Energy Loss (NIEL) dose to an expected level that should not exceed 4.0×10^9 10- MeV $protons/cm^2$ (G. Seabroke 2009). Analogous studies were presented for the satellite missions XMM and ABRIXAS (N. Meidinger, et al. 1999) and (G Y. Prigozhin, et al. 2,000)

Gaia CCD's are endowed with features specifically aimed at reducing the effects of radiation-induced charge traps: the pixel architecture incorporates a supplementary buried channel (SBC) that reduces the interaction cross section between small electron packets and traps: the CCD's also have a *charge-injection* structure on the top of the parallel registers to periodically supply calibrated amount of electrons into pixels, so as to fill and make inactive almost all the radiation-induced traps before the transit of the stars.

Besides design solutions for improving charge transfer efficiency (CTE), other counter measures were considered for in flight operations in order to mitigate the radiation damage effects, such as the adoption of a suitable level for the diffuse optical background (DoB) signal to fill the charge traps. The potential benefit of DoB has been assessed through laboratory tests (see, C. Vitel (2006), L. Georges (2007) and L. Georges (2008)), together with the actual consequences of the radiation damage.

This paper presents our analysis of radiation test campaign CCN10 executed by EADS Astrium

Toulouse under ESA contract. The main objectives were:

- Measure the PSF centroid (location) shift (bias) and charge loss as a function of signal level,
- Investigate the possible mitigating role of diffuse optical background,
- Provide experimental evidence toward the development of mathematical models (and therefore algorithms) to simulate and possibly calibrate the radiation damage effects

In Section 2.1, we detail on the available data, describing the data reduction model and approach; the results of the data analysis are presented in Sect. 4, where the consequences of CTE degradation, induced by radiation damage, suffered by astrometric and photometric measurements are discussed separately. The aim is to characterize charge loss, proxy for photometric bias (L. Corcione et al. 2009) and centroid bias, the analogue for astrometry (J. C. Terrazas 2010) as functions of signal brightness. This would provide empirical evidence for calibrating radiation damage models that could be employed for bias removal during processing of the Gaia data,

2.1. Test CCN10 radiation experiment

The European Space Agency asked Astrium, (French-based company responsible for the Gaia satellite), to investigate the impact of solar flare protons on the astrometric and photometric performances of the focal plane CCDs.
Several Radiation Test Campaigns (RTC) were have been conducted by Astrium, experimenting different laboratory strategies for mitigation the impact of the damage radiation and reduce pernicious effects during the operational life of the Gaia satellite.
An equivalent fluence dose of 10 MeV protons has been defined to represent, for the purpose of this experiment, the complex radiation input expected to be received by the Gaia detectors throughout the mission lifetime.

We report here on our own independent investigation of the experiment called CCN10 designed to analyse radiation-induced charge loss and centroid bias in the astrometric payload, and to what extent different levels of Diffuse Optical Background (DoB) might help with mitigating the damage.

Independent to another studies elaborated at the same Radiation data set by diverse hight researchers by ESAs Gaia community, our studies extend the analysis inside the photometric and astrometric performance providing some additional contribution such are the study of the "tilt distortion regarding the Mask centroid Bias, as well as an extension in study of the radiation induced consequences" in the others.

A full description of the test set-up are given in the test report by Astrium ((C. Vitel 2006)), that also gives the results of Astrium's own analysis. Hereafter, we recall the relevant features of the experiment, that will help the reader in understanding the current analysis.
The CCN10 test was carried out with the typical Gaia CCD, which had been previously exposed to proton irradiation of different intensity across the CCD area, according to an irradiation scheme agreed between ESA and Astrium. Following the across scan direction, from top to bottom, one third - about 600 lines (i.e., 20 $[mm]$ in size) - of the CCD sensitive area was kept shielded from proton radiation by an aluminium plate, the middle section of the same size, from line 650 to line 1.250 - received $4x10^9\ protons/cm^2$ equivalent dose, which corresponds to the predicted amount of 10-MeV protons received at the end of the five-year operational life. The remaining 20 $[mm]$ area, from line $1,400$ to line $1,966$ was irradiated at the level of $1 \times 10^{10} protons/cm^2$.

In between zones, there is the *transition area*, where the radiation level changes progressively in an unpredictable way. The CCD was operated, electrically and thermally in nominal flight conditions; measurements were taken at 165 K and in TDI readout mode with a pixel frequency of 80 KHz for the image area and of 400 KHz for the readout register. PSFs were simulated by using an optical mask with 14 pinholes (ref figure 2) arranged in two columns, which were almost aligned orthogonally (across-scan - AC - hereafter) to the TDI motion versus (along-scan -AL- hereafter); our analysis employs only the 10 leading pinholes of the first column, spots labeled by Astrium from A to J (Figure 2(a)). The data set comprises 20 TDI transits of the mask for each

of six signal levels, corresponding nominally to $60,000$, $7,000$, $2,000$, 650, 400, and 200 electrons, integrated along a CCD transit (i.e., $4,500$ TDI steps $= 4,42\ s$).
According to the applicable Gaia configuration at the time of the $CCN10$ data, the adopted signal intensities would span a magnitude range from $V = 13$ to $V = 22$. Measurements at each signal level were repeated for three different levels of DoB: namely at the level of 0, 5 and 10 electron/pixel.

During each TDI transit, the mask was placed in front of the CCD covering a strip of parallel registers ranging from the non-irradiated area to the $4 \times 10^9\ protons/cm^2$ irradiated region: light spots from A, B, C, and D transited over the non-irradiated zone; while, spots from E, F, and G passed over the transition zone between the non-irradiated and irradiated mid-section, spots H, I, and J passed entirely over the 4×10^9 irradiated zone.
Image-spot from pinhole D slightly overlaps the transition zone, and so it is expected to experience partial irradiation. A set of 20 TDI transits at a high signal level, i.e. $60,000$ electrons, each PSF placed in the un-irradiated region make also part of the delivered data set a reference data for calibration purposes. Simulated PSFs, spreading over a 12×12 pixels window, are all binned across-scan at CCD readout node, so a total of $3,600$ individual simulated Line Spread Functions (LSFs) - 15 AL pixel in size - need fitting per each measurement session with a given intensity signal and DoB level.

3. Measurement analysis

3.1. Measuring model

There are two possible alternatives for analyzing our experimental data: a non-parametric approach, like, e.g., the method based on the Cramer-Rao limit proposed by (R. Mendez, et al. 2013) in the context of accurate CCD measurements, and a more traditional functional-fitting model. We decided to adopt the latter for the difficulties, in a non-parametric framework, of taking proper account of any spurious (systematic) contribution, given the limitations of the experimental set-up, which was known to have been executed with a loose control of the stability and repeatability of the light source, and of the mechanical positioning of the mask.

Our analysis was then performed by fitting the following Gauss function to the sampled LSFs: in order to estimate the image parameters from both non-irradiated (the reference case) and irradiated data:

$$y = y_0 + \frac{A_0}{w\sqrt{\frac{\pi}{2}}} e^{-2\frac{(x-x_0)^2}{w^2}} \tag{1}$$

where the fit parameters have the following meaning:

y_0 = offset, which is equivalent to the background

x_0 = peak location, (i.e., image centroid)

w = twice the standard deviation of sample distribution corresponding roughly to 0.849 FWHM (Full Width Half Maximum)

A = total area under the curve above the background (i.e. integral flux).

Such a Gaussian profile is not the most accurate modeling function for damaged image profiles, for which other fits based, e.g., on splines, are certainly better. However, all we need here is a simple and robust estimator suitable for accurately comparing estimated image parameters (location and integral flux in particular) from both non-irradiated (the reference case) and irradiated LSF data, and the adopted Gaussian function is certainly up to the task.

The Gauss spot brightness (i.e., the integral flux) from the reference, non-irradiated, data set are used to calibrate the brightness from the irradiated session, so as to compensate for the signal variation across the mask due to the light source distribution. Then, the charge loss, associated to the radiation-induced Charge Transfer Inefficiency ($CTI = 1 - CTE$), is computed by linking the calibrated brightness of the spots passing across the irradiated CCD parallel registers to the ones traversing the non-irradiated parallel registers.

Concerning the astrometric calibration, the Gaussian location is first used to fit reference, non-irradiated data, so as to investigate on the repeatability of the experiments and to assess those components, i.e. tilt and distortion, of the centroid bias related to the opto-mechanic set-up, or

mask bias (as it also called in this article). The centroid bias associated with the radiation damage is then obtained by first linking the Gauss centroid positions from the LFS samples in the irradiated region of the CCD to the reference centroids from the non irradiated LSF samples, then compensating the results for the mask bias.

The availability of different experiment sessions executed with different signal intensities and DoB levels allows eventually to correlate the charge loss and centroid (location) bias to the signal strength and to the added background signal, and to infer the possible curative role of DoB against the radiation damage.

3.2. Experiment Photometry

The average spot intensities from the Gauss fit, i.e. the gauss area of each spot averaged over the number of transits, are first used for a quick check on the data set quality and a very qualitatively assess of both the charge loss affecting the spot signal across the damaged area and the effectiveness of the DoB in healing the CCD from radiation damage; such a preliminary analysis also serves to understand how to properly calibrate spot brightness for a more detailed investigation on the relationship between the charge loss, spot intensity and DoB.

A first goodness check has been accomplished by computing the LFS profile contrast, i.e. the Signal to Noise Ratio (SNR), for all leading image spots:

$$SNR = \frac{n_{signal}}{\sqrt{n_{signal} + (V * 15)}} \qquad (2)$$

The SNR makes use, as source signal of the integral of the Gauss fit, where n_{signal} is the area under Gauss fit, and the total noise is the sum of the Poisson noise of the source and the background noise. The background noise associated to the source is the product of statistic variance of the background times the quoted source size, i.e. $15-$pixel LSF window: the variance V is the `rms` of signal over the first $4,500$ TDI steps preceding the simulated star imprints, and it encompasses background signal photon noise and electronic readout noise (RON). The SNR estimates for the whole irradiated data set are shown in Tables 2, 3 and 4. All LSF profiles are well above of the comfortable detectability threshold, i.e. $S/N = 3$, even at lowest light exposure ($S = 200$) equivalent electrons.

The SNR is mainly dominated by the signal power; the extra noise contribution from the DoB - integrated over the $15 \times 15 - pixel$ signal window - is the main reason for the noticeable decrease of the SNR from null DoB case down to $DoB = 10$ case, which affects the measurements at every illumination level from $S = 200$ to $S = 60,000$.

As the signal level increases and the background noise contribution becomes more and more negligible, measurements approach the photon noise limited regime and SNR values get very close to the square root of the star signals. This trend applies to all measured leading spots, independently of the illumination signal power; spots D, E, and F are always in photon noise limited regime, independently of the illumination level, as a consequence of the light distribution across the mask which peaks close to pinholes D and F.

Such a feature of illumination distribution is common to every measurement session (see Fig. 3); it is likely associated to the optical set-up of the experiment, which is actually affected by a non-uniform optical quality across the field.

Comparison of the scan-averaged Gauss brightnesses from the different test sessions also reveals the lack of a control of the stability of the external light source, which significantly varies from session to session with nominally equivalent illumination levels: the signal power variation is more evident for the cases with $S = 60,000\ e^-$, including all the DoB sessions and the reference set (see Fig.3).

The significant fluctuation of the signal power across the mask and between test sessions makes the signature of charge loss due to the radiation-induced CTI apparent only for the brightest sessions with signal power $S \geq 2,000e^-$), for which the plots of the plain Gauss brightness (reffig:BrightnessCurves) show a clear change in shape for spots in the irradiated area of the CCD, with respect to the trend draw from the spots in the non irradiated region; at fainter signal levels, the charge loss signature in the brightness curves almost vanishes, particularly for the cases with $DoB = 5$ and $DoB = 10$.

By the current photometric accuracy, it is very instructive to investigate on the charge loss occurring scan by scan, at least for the brightest ses-

sions - $S = 60,000$ and $S = 7,000$ - which show a measurable signature of trap activity. The computation involves the differences of the Gauss spot brightness in every scan with respect to the value in the preceding scan, $S(n)-S(n-1)$, and the outcomes are shown in Fig. 4 for the representative case with null DoB, so as to also avoid any possible mitigation from the extra background signal.

From the case $S = 60,000$ which has the more intense charge loss signature (Fig. 4, left panel), the signal differences of simulated stars in the non-irradiated area (A, B and C) are close to zero, confirming as this region is not affected by radiation damage. Star D, passing along the edge of the non-irradiated and the transition zone, seems to experience a moderate trap activity in between the first and the second run. The trap effect, i.e. the radiation damage, progressively increases down the transition area, and brings stars F and G (closer to the border with the $4E9$ zone) to a signal reduction comparable with the first star - star H - fully embedded in the irradiated zone. The last stars I and J in the 4×10^9 zone show the same charge loss during the first two transits, but the reduction is significantly lower than the one which occurs for star H in the same area.

The charge loss amount for spots over the irradiated area and in the transition zone strongly correlated to signal intensity. The image spots from E to J, spanning over the transition zone and the irradiated area, suffer a further reduction of charge, though smaller, between the second to third passage. After the third run, the statistical fluctuations of the residual trailing charge for the perturbed stars is noisier than the ones associated to undamaged stars A, B and C, likely a consequence of stochastic processes of release and capture of charge taking place in between runs. The trap activity affect also the experiment with $S = 7,000$; although for such a case, the measurements are heavily dominated by signal fluctuation among scans (Fig. 4, right panel).

The trend of charge loss, scan by scan, also reveals the healing role of the self-injection, by which the charge injection into damaged pixels due to the first transiting stars paves the way to stars in subsequent scans, which are no longer (or much less) affected by traps; this is likely the consequence of the fact that most of the traps are "slow" traps, featuring a typical release time constant longer than the 30-*seconds* interval between scans.

Non-uniform illumination across the mask and the light source fluctuation during test sessions, need to be compensated for by an appropriate brightness calibration in order to achieve meaningful evaluation of the radiation-induced charge loss. The photometric calibration is performed by flat-fielding the plain average Gauss brightness to the equivalent measurements of the reference, non-irradiated sessions: every star signal, from the irradiated case is divided by the corresponding value from the non-irradiated test, and the result is rescaled to the mean brightness, across the mask, of the reference.

$$S_i^{cal} = \frac{S_i}{S_i^{ref}} \times \widehat{S}^{ref} \tag{3}$$

Flat-fielding results for all illumination levels are shown in Figs. 5, 6, and 7, for sessions with $DoB = 0$, $DoB = 5$, and $DoB = 10$, respectively: the calibrated brightness distribution across the mask for all the illumination levels are shown in logarithmic scale (left panels); at the same time, the linear scale is more appropriate to compare the low signal level cases (right panels). The calibrated intensities allow a straight comparison of the CCD response across the mask, during the DoB sessions.

For nominally equal illumination levels $S = 7,000$ and $S = 60,000$, the measurements with $DoB = 0$ (the earliest measurement batch performed) exhibit actual intensities significantly lower than those of the sessions with $DOB = 5$ and $DOB = 10$, performed one month later.

At low illumination levels, from $S = 200$ to $S = 2,000$, the brightness levels for the three DoB sessions are comparable. The most noteworthy difference among sessions is the drop of the signals for image spots H through J passing over the $4x10^9$ irradiated region, with respect to the mean signal of spots A through C in the non-irradiated area.
For the null DoB session, the signal drop - i.e. CTI charge loss signature - is clearly measurable at all illumination levels. As the background increase,the signal variation across the mask significantly reduces for all illumination levels, and almost vanishes at very low signal regime (Figs. 6 and 7, right panels): measurements for $DoB = 5$

session with $S = 200$ show a very marginal but still clearly measurable signature of the trap activity in the irradiated region; at the equivalent illumination level but with $DoB = 10$, the trap effect is less evident and the charge loss signature is more ambiguous. We assume that charge loss is still present but covered by noise.
The response of the CCD irradiated region is further discussed in the Sect.4.1, through quantitative evaluation of the charge loss across the mask and as a function of the signal intensity.

3.3. Mask centroid bias: tilt and distortion

The reference data set (i.e. the sequence of 20 passages of the mask over the non-irradiated area of the CCD with nominally non damaged pixels, executed at signal level close to $60,000\ e^-$ and null DoB) allow to assess the opto-mechanic features of the experiment, which are crucial for an accurate calibration of the centroid bias ultimately related to the radiation damage. In this respect, it is reckoned very relevant to investigate the repeatability of mask position on the CCD and to possibly quantify all the components affecting the centroid position, which are likely associated with the mask machining and optical variations and/or distortion.

The analysis of scan-averaged Gauss centroids for the reference case (Fig. 8, left panel) allows to clarify the various effects that degrade the accuracy of the mask positioning during scans. The actual tilt of the mask, order of 0.55 Al pixel (i.e. 32 *mas* on sky as the difference between the AL positions of spots A and J) as anticipated and also measured by Astrium ((C. Vitel 2006)), is confirmed. The mask initial position, scan by scan, is affected by an AL positional jitter as large as 0.5 AL pixel.

A more in-depth analysis through the linear fitting to the AL positions of specific reference spots - pinhole imprints from A to C are used, so as to be consistent with the execution of the irradiated sessions - better clarifies the contribution to the AL shift of the spot position due to the mask. The mask tilt, i.e. the AL shift between the positions of the stars A and J along the fitting straight line, is actually slightly larger, i.e.average order of 0.611 AL pixels or 0.36 *mas*, than the raw estimate above. Besides the linear component of the mask tilt, the AL shift of the spot positions also include non-linear terms possibly associated with either an inaccurate mask machining or a field distortion of the optical set-up of the experiment.

The shape of such a distortion is obtained by compensating the spot centroids for the mask tilt from the best fitting straight line of the positions of the first pinholes A to C, the result is shown in Fig. 9 . The curves of the AL shifts of the spot positions, scan by scan and after removing the mask tilt associated with the individual scan (Fig. 9, left panel) show similar shapes scan after scan, and undergo an almost "rigid rotation", which is presumably the result of a mechanical yaw, as large as 0.14 AL pixel peak-to-valley, affecting the mask movement during transits.

The average mask centroid bias (Fig. 9, right panel), i.e. the AL positional shift presumably associate to the intrinsic mask geometry and/or other repeatable - e.g. optical - distortions of the experimental set-up, is obtained by averaging over the number of scans the residual of the spot Gauss centroids with respect to the average mask tilt from the average linear fit of the positions of the reference spots from A to C.

In order to investigate the repeatability of the AL position of the mask throughout the whole CCN 10 campaign, the absolute spot positions, averaged over the number of scans, for the $S = 60,000$ irradiated sessions, are compared with the reference session executed in equivalent nominal illumination conditions; the linear best fit to the averaged positions of star A to C in the non-irradiated zone, is also employed as a distortion free reference: the plots are shown Fig. 10, where the graphs of the irradiated sessions are translated along the vertical axis to superimpose to the reference case, so as to allow a straight comparison among the different trends.

The plots allow disentangling some of the effects that make the assessment of the CTI centroid bias problematic, the most relevant are the mask position variation, over a range as large as 2 AL pixel, among the considered sessions and the progressive departure of the centroid positions of the reference session from the best fit line as the consequence of residual non-linear opto-mechanic distortions of the experimental set-up.

4. Radiation induced effects

4.1. Charge loss

The usage of not calibrate photometry does not allow to achieve un-ambiguous measurement of the charge loss amount at every illumination level, and consequently a meaningful conclusion concerning the effect of radiation damage on the measured signal. From the flat-fielded brightness distribution across the mask (Figs. 5, 6 and 7), the average charge loss, due to radiation damage, as a function of the position on the mask, i.e. across CCD areas, is obtained from the difference between the spot intensity and the average signal level of image spots A to C in the non-irradiated CCD area.

Such an approach leads to the results shown in Figs. 12, 13, and 14 , which illustrate how the integral and relative amount of charge loss vary across the field for all illumination levels, during the different DoB sessions. Note the adoption of a logarithmic scale in the integral charge loss (left panels) so as to better determine the integral charge loss trend. Negative values, due to the signal statistical fluctuation in the non-irradiated region (stars from A to C), are not representative of the effect of the radiation damage and are removed from the plot by truncation at the 1 electron threshold. The behavior across the whole CCD exposed area is most apparent from the relative charge loss graphs (right panels).

The plots of integral and relative charge loss confirm and quantify the very different behavior of the CCD during DoB sessions, which was anticipated qualitatively by the calibrated photometry results in Sect.3.2.

$DoB = 0$ session has actually the strongest signature of the charge loss, and the measurements at the various illumination levels are very comparable one each other. In irradiated area (i.e. stars from H to J), the relative charge loss for each illumination level is distributed over the range from 30 to 40 percent of the average signal of the undamaged stars (A to C): the dispersion may be related to the measurement statistics. For the $DoB = 5$ and $DoB = 10$ sessions, the relative charge loss measurements are significantly lower than the null DoB cases, but spread over a wider range, from 25% to 10% of the average intensity. Noteworthy also is the change, between the $DoB = 5$ and $DoB = 10$ sessions, of the CCD response in the irradiated area at low illumination levels. For experiment with the $DoB = 10$ and illumination levels from $S = 7,000$ to $S = 200$, the relative charge loss drops below the 15% level, and the estimates spread from 15% ($S = 7,000$) to 3% ($S = 200$); in particular for the faintest case $S = 200$, the trap effect almost disappears and the estimated charge loss in the irradiated area is negligible, or not significantly different from the response of the transition region (Fig. 14, right panel).

Conversely, for the brightest signal level $S = 60,000$, the charge loss is reduced from $\sim 35\%$, for the case with null DoB, to $\sim 25\%$ for both cases with $DoB = 5$, and $DoB = 10$. Apparently, the diffuse optical background seems to provide some compensation for the radiation damage effects on the CTI, with performance progressively reduced at higher signal levels. The present estimates of the fractional charge loss as a function of the spot position on the CCD and of the DoB value compare very well with equivalent evaluations achieved by A. Short ((A. Short 2006)) and ASTRIUM ((C. Vitel 2006)) in their alternative analysis of same data set.

For the purpose of clarifying the DoB role in the mitigation of the radiation damage, as well as for the definition of a simple analytic description of the trap effect for CTI modelling, we tentatively provide an analytical law relating the charge loss to the signal level, i.e. the size of the charge packet collected in the CCD pixel. Previous reports of calculation algorithm for the charge transfer loss in Scientific CCD devices has been presented by N. Krause, et al , Fig. 15 shows the average charge loss as a function of the average signal, for the different DoB sessions: the plots are obtained from the measurements above, by computing, for every illumination level, the average charge loss $-y$ axis $-$ as mean of integral charge loss for the three stars H, I and J, in the irradiated CCD area, and by employing as average signal $-x$ axis $-$ the mean of the calibrated brightness of the three stars A, B and C, in the non-irradiated area.

The log-log plot evidences the straightforward relationship between charge loss and signal level, and also shows a distribution of the measurements approximately in accordance to the power law $y = aS^b$, where y is the charge loss and S the charge packet size: the best fit parameters for

such a power law are reported in Table 1, together with associated errors. The charge loss distribution functions among the different DoB sessions provide helpful hints about the possible role of the diffuse background in mitigating the radiation damage. The increase of the steepness seems correlated to the increase of the background, and steepness variation is due to the strong decrease of the charge loss amount for the faintest signals. The gap among the curves could be fully attributed to the moderate light background, whose contribution, integrated over the Gaia 15 × 12-pixel window, is estimated at around 900 and 1,800 *electrons*, respectively for the $DoB = 5$ and $DoB = 10$ cases. These results seem to confirm the effectiveness of the diffuse background in partially compensating the effect of the radiation damage, and faint sources seem to have a larger relative benefit of such a compensation (which is nonetheless larger in absolute values for brighter sources).

Nevertheless, taking also into account the temporal succession of $DoB = 5$ and $DoB = 10$ tests, performed with a short time elapse between them, and of the earlier $DoB = 0$ session, performed almost one month before, the above fitting functions could also describe different radiation damage states, as a result of an intrinsic change in the CCD due to some modification of crucial CCD operational parameters (e.g., working temperature or electric biases), which can possibly modify the radiation-induced trap density or activity. Therefore, the model most appropriate for reproducing the actual response of the damaged CCD should be evaluated in the light of the knowledge of real CCD operational state during and between test sessions, and on the impact it has on the distribution and behavior of the electron traps.

4.2. Astrometric bias

Concerning the calibration of LSF locations and the evaluation of CTI centroid bias, the analysis in Sect.3.3 has led us to the conclusion to compensate the Gauss centroids for the geometric features of the mask - tilt and distortion - in two steps: **first**, the average Gauss centroids (i.e. LSF AL positions) for each DoB and illumination level session are normalized to the average linear trend as identified by the positions of the three nominally undamaged spots A to C of the same session; **second**, the relative positions are compensated for the average mask centroid bias (see Sect.3.3), representative of the opto-mechanical imperfections as a whole, under the reasonable assumptions that the mask is rigid and the optical setup does not change significantly throughout the test sessions. The results of the individual steps of such an approach are shown in Fig. 16, separately for different signal levels. The left panels show the centroid positions corrected for the mask tilt applicable to the session; the mask bias (see Sect.3.3) is also shown as solid black line. Right plots display the position shifts after the compensation for the mask bias.

The consequences of the radiation damage on the LSF position shift across the differently irradiated areas of the CCD are already evident once the mask tilt is compensated for: however, further removal of the opto-mechanical distortion, i.e., mask bias (see Fig. 9), is decisive for accurately quantifying the centroid shift linked to the CTI effects. After the compensation for both components of mask geometric features (i.e., tilt and distortion), the CTI centroid bias (Fig. 16, right panels, position residual associated to the radiation induced CTI effects) progressively increases from an almost null value, for spots - A to C - in the non-irradiated area, to a quasi constant value for spots H to J, in the $4E^9$ irradiated region, where the position residual depends on the illumination level: the brighter the source, the larger the position shift . Such a trend is very well defined for all the brighter sessions ($S \geqslant 2,000$); for the fainter sessions ($S \leqslant 650$), the LSF position shift measurements in the irradiated region scatter over a range as large as 0.1 AL pixels, as a result both of the mask positioning error (Sect. 3.3) and of the reduction of SNR which affect the centroid estimates (Fig. 11 on 14).

A comparative analysis among sessions with different DoB levels, see Fig. 16, reveals that the moderate DoB levels, 5 and 10 *electron* per pixel, actually provide a detectable mitigation of the position shift associated to the radiation damage, in particular for the cases with source brightness $S \geqslant 2,000$, for which the addition of the DoB produces a significant reduction, correlated with the DoB value, of the position shift in the irradiated region of the CCD.

For the measurements at low source brightness,

i.e., $S \leqslant 650$, the DoB role in partially compensating the CTI centroid bias is not so evident as for the brighter cases, likely as a result of the inaccuracy affecting the centroid estimates for fainter sources, dominated by the additional noise from the background signal (see Fig. 11 on 14). Only the sessions with $S = 650$ show an evident mitigating role of the DoB; which, independently from the applied signal intensity either 5 or 10 *electrons* per pixel, is capable to recover almost the whole amount of the positional shift affecting the spots, from D to H, onto the irradiated area of the CCD. In order to clarify the usefulness of the DoB for the CCN10 test, which search mitigate the radiation effects, it is convenient to represent the estimated centroid bias, as a function of the source intensity, for each adopted DoB configuration.

The relation of the centroid bias against signal brightness (Fig. 17) is obtained by comparing the LSF positional shift (Fig. 16), corrected for the positional effects of the opto-mechanic setup, with the average non-irradiated signal signal brightness from the photometric analysis (Sect. 3.2).

The relations between the radiation-induced LSF position shift and the signal brightness can be split in two signal domains. In the fainter signal regime, $S \leqslant 650$, the position shift undergoes a steep decrease as the signal increase; such a trend seems well defined for the measurements with $DoB = 0$ and $DoB = 10$. The potential mitigation of the CTI effects by the DoB is revealed by the noticeable gap, of the order of 0.02 AL pixels almost constant along the considered signal range, between curves for sessions with null DoB and $DoB = 10$. Unfortunately, measurements with $DoB = 05$ depart from the observed trend for the other DoB cases, presumably because of some unpredictable opto-mechanical changes in the experiment setup which perturb the centroid estimate, and are not compensated for by the adopted data processing approach; the discrepancy makes any conclusion very preliminary.
At brighter signal levels, $S \geqslant 2,000$, the centroid bias is well correlated with the signal intensity, and apparently the shift amplitude scales proportionally with the logarithm of the source brightness. In this signal range, the addition of a moderate signal background, $DoB = 05$ cases, makes the shift reduce by an amount of the order of 0.05 AL pixel (≈ 3 *mas*), almost constant over the brighter signal range. Apparently, increasing the DoB level, $DoB = 10$ cases, does not produce any further unambiguous healing effect.

It is worth noting how the change from negative to positive steepness of the CTI centroid bias curves seems to occur at an integrated signal value very close to the saturation level - quoted as large as $1,800$ electrons - of the Supplementary Buried Channel (SBC), which is implanted in the Gaia CCD pixel so as to improve the radiation hardness of the device. The observed behavior of the CTI cetroid bias could be tentatively accounted for in the light of such a complex Gaia CCD pixel architecture.
Small charge packets, up to $1,800$ *electrons* in size, are fully transported through a narrow stream confined to the SBC; the traps in the reduced volume of SBC get almost completely filled at relatively low signal, and consequently the centroid bias decreases as the charge packet increases, up to reaching the minimum when the pixel begins to operate close to the SBC saturation mode.

As the charge packet size exceeds the SBC saturation level, the charge excess uses a larger and larger portion of the regular buried channel, and in turn an increasing larger number of traps, which are responsible for the LSF position shift increase in the brighter signal regime. For the sake of comparison, Fig. 18 below shows the relation centroid bias vs. signal intensity obtained by independent analyses carried out on the same data set ((A. Short 2006) and (S. Brown & F. Van Leeuwen 2008)). Our estimates of the CTI centroid bias basically confirm the behavior reported by Short; in particular, when results by similar fitting curves are considered (Fig. 18, black and blue lines), our analysis compares well with Short's over the whole interval of the considered signal intensities. The comparison to Brown's results (Fig. 18, red lines) is more problematic.

The two analysis provide comparable estimates of the CTI centroid bias for the brighter sources ($S \geqslant 2,000$), but they significantly differ in reproducing the centroid bias in the low signal regime for $S \leqslant 600$. Brown's analysis provides a very high values of the positional shift for the fainter sources, which seems to suffer a shift as large as that experienced by the brightest sources, i.e., $S = 60,000$. Furthermore and very unexpectedly, Brown's mea-

surements with $DoB = 10$ provide negative bias value for the faint sources, compatible with LSF leading edge distorted by a charge excess; this might be explained by the different methods for normalizing and correcting the systematic errors.

5. Conclusions

All CCN10 test sessions were executed in adequate SNR regimes, inclusive of the one with moderated illumination power, and measurements exhibit SNR larger than the detectability threshold (e.g., SNR > 3) in almost all cases.The radiation damage effects are clearly shown by the evolution transit by transit, of image spot brightness across the irradiated area.

The charge loss due to trap presence affects the simulated star signal mostly at the first transit; a further, less intense charge loss can occur at the second transit, when the signal intensity at the first transit was not powerful enough to saturate available traps. Such a behavior indicates that the traps involved are very effective in capturing electrons and less in releasing them: i.e. they are slow traps, whose average release time constant is longer than the interval between transits ($30[s]$).

The average amount of charge loss is highly correlated with the signal intensity, in accordance with theoretical predictions that relate the trap behavior, (e.g., time capture constant), to the electron density in the pixel. Unfortunately, the large and unexplained discrepancy in the CCD response in different test sessions does not allow the identification of a simple analytic law for the charge loss as a function of the integrated signal, capable to reproduce the behavior of the damaged CCD (having experienced a radiation dose equivalent to the expected Gaia end-of- mission level, i.e. 4×10^9 $protons/cm^2$).

The current results allow only to state that the charge loss measurements follow a power law $y = aS^b$ (see Figure 15), whose parameters can vary over large ranges, as a possible consequence of variation of the diffuse optical background and of the CCD operational parameters. The large spread involved point to the need for a careful assessment of the actual analytic model of charge loss, based on a much better knowledge of the real experimental conditions, and of the possible changes induced on the detector.

The adopted levels of DoB apparently contribute in partially mitigating the radiation damage, and the benefit in terms of decrease of the charge loss amount is particularly evident in the case of the faintest signal levels. This also suggests that an appealing alternative to diffuse optical background for trap filling and mitigation of radiation damage effects is charge injection, performed at a comparably low rate (e.g., once every several minutes), with an intensity comparable to the high end of the detector dynamic range.

The centroid analysis demonstrates that the CCN10 test was executed with a rather loose control of the mechanical positioning of the mask (Figure 9). The large mask initial position jitter (as large as 0.5 AL pixels rms) and the mechanical yaw (of the order of 0.04 AL pixel rms) makes the LSF location measured in the non-irradiated test session unreliable as reference position for assessing the CTI-induced position bias.

The most relevant information, useful for the centroid bias calibration, that the non-irradiated session can provide, is the amount of intrinsic mask distortion (Fig. 9) i.e., the contribution to the LSF position shift due to both the mask machining and residual optical distortions, which can affect the LSF location by shifts as large as 0.06 AL pixel at the maximum extent, which corresponds to the spots in the $4x10^9$ irradiated zone.

Once the irradiated LSF positions are properly compensated for the actual mask geometric bias (i.e., tilt and distortion), the centroid residuals provide a reliable estimate of the position bias associated to the radiation damage, i.e. the CTI-induced astrometric bias.

In agreement with the results of other analysis, the correlation of the measured CTI centroid bias with the calibrated brightness proves that the addition of a moderate DoB is a viable solution for mitigating the CTI effects in the brighter signal regime ($S \geqslant 2,000$): $DoB = 05$ $electrons$ per pixel provide a noticeable reduction, of the order of 0.05 AL pixel (≈ 3 mas) of the position shift, but the increase in the background signal, up to 10 electrons per pixel, apparently does not give any further improvement.

The measured centroid bias at low signal levels, i.e., up top the values comparable with the

quoted saturation level - $1,800$ *electrons* - of the SBC, demonstrates the effective role of the SBC in hardening the CCD against the radiation-induced CTI effects for the faintest signals; unfortunately, the lack of measurements with source power in the range between $S = 650$ and $S = 2,000$ *electrons* does not allow to definitively clarify the role of the SBC, in terms of achievable astrometric accuracy in presence of radiation damage, for signal intensity close to the expected Gaia limiting magnitude $G = 20$, i.e. ≈ 810 $photo - electrons$.

This work was supported by the Italian Apace Agency (ASI) under contract $I/058/10/0$

REFERENCES

Brown, S. & Van Leeuwen, F., 2008, "Analysis of the CCN10 data set: CTI effects on a Gaia astrometric CCD"

Brown, S. & Van Leeuwen, F., 2009, "Further analysis of Radiation Campaign 1: an extension to SWB-001"

Corcione, L. et al., 2009, "CCN10 radiation test campaign data: photometric performance and charge loss in Gaia irradiated AF CCD"

Georges, L. et al., 2008, Technical report "Radiation campaign 3. Astrium bench characterization tests report", EADS - Astrium

Georges, L. et al., 2007, Technical report "Radiation Test Campaign 2", EADS - Astrium.

Georges, L. et al., 2008, Technical report "RTC3, Bench characterization data delivery", EADS - Astrium

Gregory Y. Prigozhin, et al., 2,000. "SPIE, X-Ray and Gamma-Ray Instrumentation for Astronomy XI", 4140. 123.

Hopkinson, G.R., 1996, "Proton effects in Charge-Coupled Devices", "IEEE Transaction on Nuclear Science", 43, 614.

Krause, N., et al, 2,000. Nucl. Phys. A, 439, 560-566.

Meidinger, N., et al., 1999, Nucl. Phys. A, 439, 319-336.

Mendez, R., et al. 2013, "Analysis and Interpretation of the Cramr-Rao Lower-Bound in Astrometry: One-Dimensional Case ", THE ASTRONOMICAL SOCIETY OF THE PACIFIC, 125, 580-594.

Pasquier, J. F. et al., 2011, Technical Report "Radiation campaign #5 tests plan" EADS - Astrium.

Perryman M., 2009, Cambridge University Press ISBN 978-0-521-51489; Astronomical Applications of Astrometry "Ten Years of Exploitation of the Hipparcos Satellite Data"

Seabroke G. et al., 2009, "Modelling radiation damage to ESA's Gaia satellite CCD's", SPIE volume 7021.

Short, A., 2006, "Independent Analysis of EADS Astrium CCN10 Radiation Test Data", "Advanced Concepts, Science Payloads Office, ESTEC, ESA"

Terrazas V, J.C. et al., 2010. "Astrometric performances of Gaia irradiated AF CCD from CCN10 radiation test campaign data analysis"

Vitel, C et al., 2004, Technical Report, "AFCCD characterisation tests phase-Back Illuminated CCD Test Report", EADS Astrium

Vitel, C., 2006, technical report "CCN10 radiation test", "EADS Astrium"

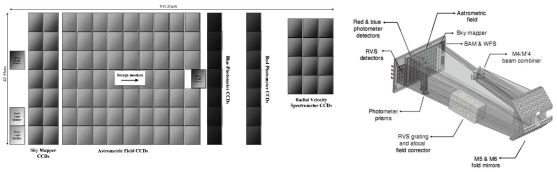

Fig. 1.— Gaia telescopes and focal plane: the fields of view of the two telescope are mapped to a common focal plane made of 106 large-format CCD's, each with 4,500 TDI lines, 1966 pixel columns, and pixels of size 10 μm along scan $\times$ 30 μm across scan (59 $mas \times 177$ mas on sky). Star images cross the focal plane in the direction indicated by the arrow, the along scan versus across scan.

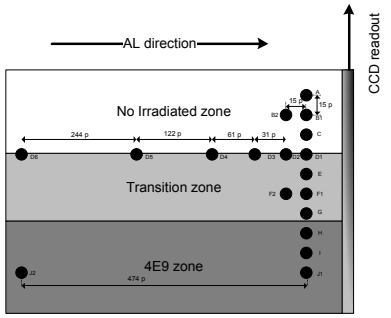

(a) CCN10 configuration

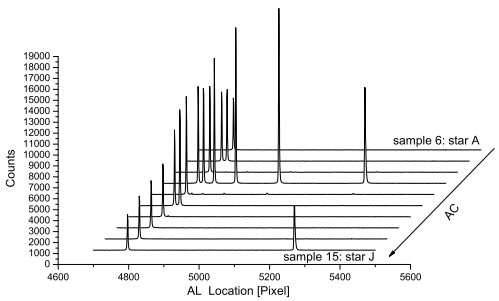

(b) LSF location AL and AC in a simple run.

Fig. 2.— CCN10 Mask pattern design

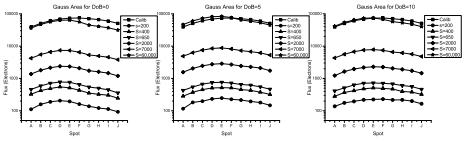

Fig. 3.— Image spot brightness during CCN10 test sessions

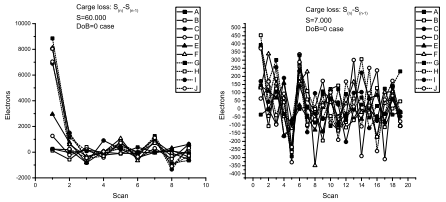

Fig. 4.— Charge loss signature scan by scan during sessions with null DoB and illumination levels corresponding to $S = 60,000$ (left) and $S = 7,000$ (right) electrons

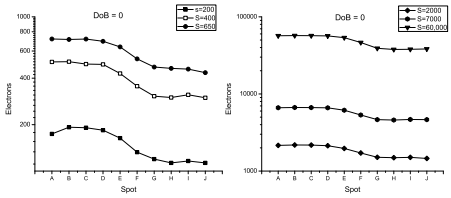

Fig. 5.— Gauss brightness flat-field to the reference case for $DoB = 0$ session: brighter cases, $S \geq 7,000$ levels (right); fainter cases, $S \leq 650$ (left)

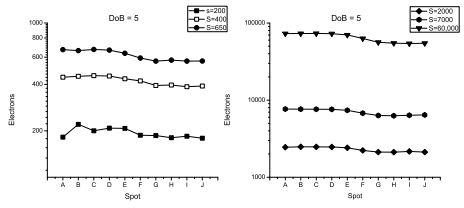

Fig. 6.— Gauss brightness flat-field to the reference case for $DoB = 5$ session. Left panel: fainter illumination levels; right panel: higher illumination levels (right).

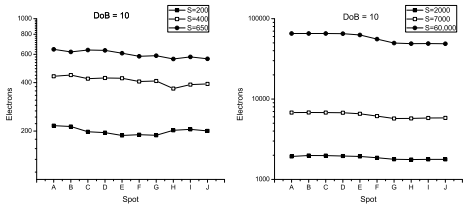

Fig. 7.— Gauss brightness flat-field to the reference case for $DoB = 10$ session. Left panel: fainter illumination levels; right panel: higher illumination levels (right).

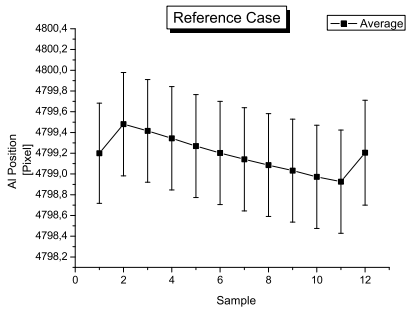

Fig. 8.— Average centroid positions across the mask for the reference sequence: leading stars from A to J corresponds to holes 2 to 11; hole 1 and 12 are imprints of mask defects and are no longer considered in the current analysis

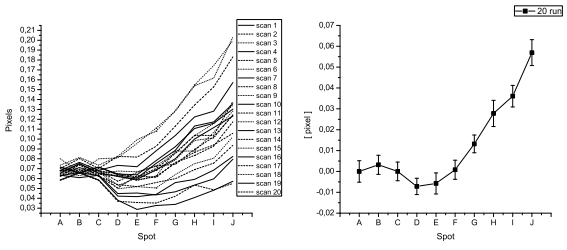

Fig. 9.— The mask centroid bias after compensating the Gauss centroid locations for the mask tilt, i.e. best fitting straight line: individual scans, left panel; average bias normalised to the position of star A, right panel.

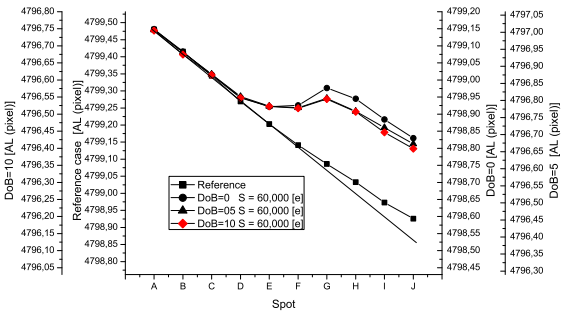

Fig. 10.— Absolute centroid positions for the reference case and DoB sessions with $S = 60,000$; the black straight line represents the nominal mask tilt, i.e., linear best fit of the positions of the spots A to C in the reference test. Measurements from irradiated cases are vertically translated to superimpose to the reference ones.

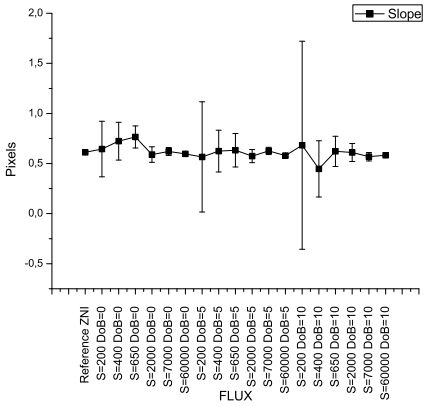

Fig. 11.— Mask tilt variation during CCN10 test sessions: scan averaged AL shift between positions of spot A and J along the average linear best fit of the non-irradiated positions A to C; the average tilt from the reference session is also shown. The increasing error for the faintest sessions ($S < 600$ electrons) is correlated with the decreasing SNR, as shown in Tables 2, 3 and 4

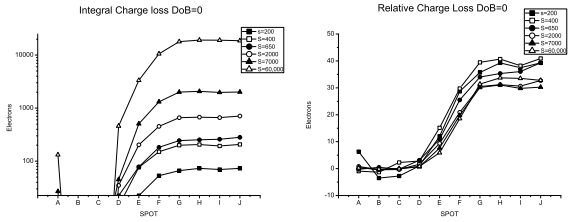

Fig. 12.— Charge loss across the mask for $DoB = 0$ cases, all illumination levels: integral (left) and fractional (right) charge loss by using as reference signal the average from image spots A to C, transiting over non-irradiated pixels.

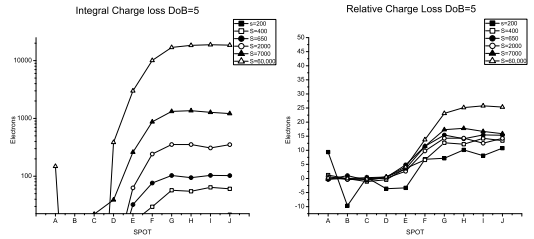

Fig. 13.— Charge loss across the mask for $DoB = 5$ cases, all illumination levels: integral (left) and fractional (right) charge loss by using as reference signal the average from imaged spots A to C, transiting over non-irradiated pixels.

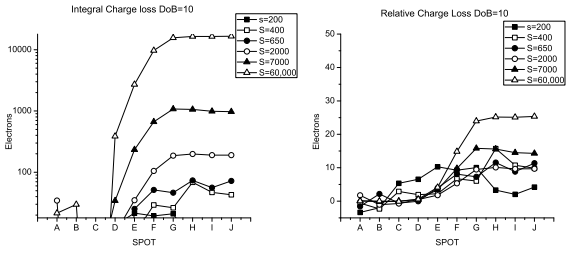

Fig. 14.— Charge loss across the mask for $DoB = 10$ cases, all illumination levels: integral (left) and fractional (right) charge loss by using as reference signal the average from image spots A to C, transiting over non-irradiated pixels.

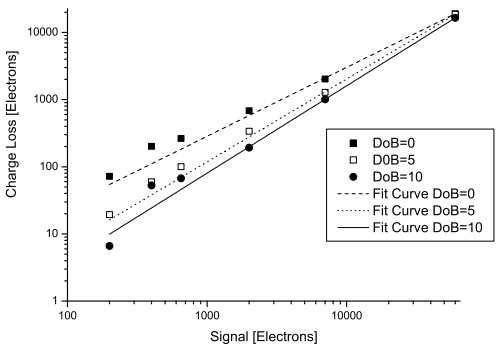

Fig. 15.— Charge loss as a function charge packet size for every DoB session; best fit curves of the measurements by the power law $y = aS^b$ are also shown.

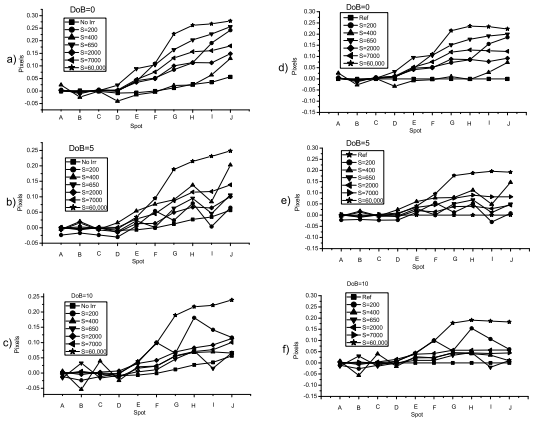

Fig. 16.— Average centroid bias across the mask as measured during the various DoB sessions, inclusive of the reference measurements in black square, representative of the mask distortion: compensated for the mask tilt (left panels); also compensated for mask distortion (right panels)

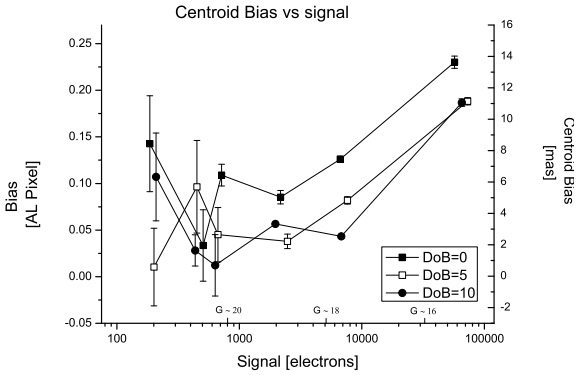

Fig. 17.— Average centroid shifts of the irradiated spots (H to J) as a function of the average brightness of non-irradiated spots (A to C) for different DoB sessions: the position shift is shown in AL pixel unit (left vertical axis) and milliarcseconds (right vertical axis); error bars show the bias rms computed over the number of mask passages performed in each test session.

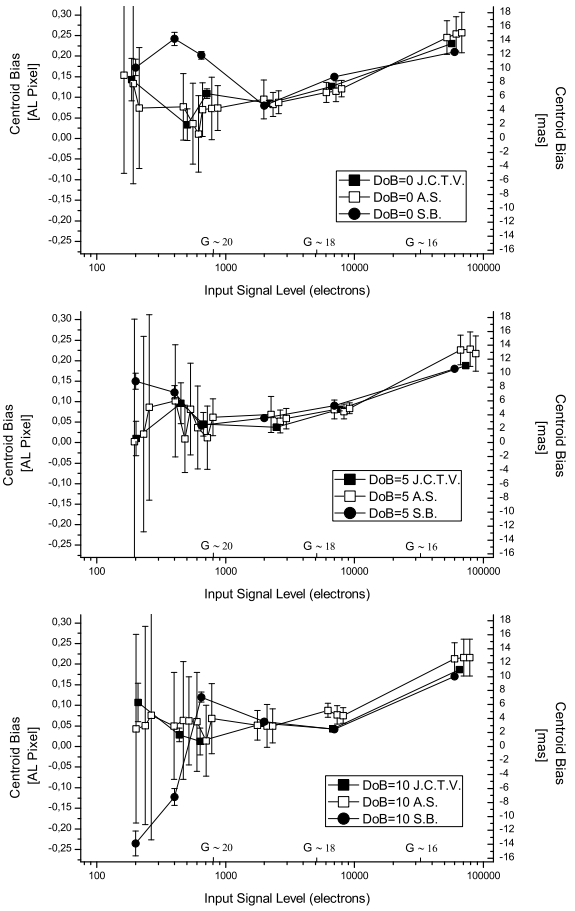

Fig. 18.— CTI centroid bias from independent analyses of CCN10 campaign, arranged for the increasing DoB level from top to bottom: our results are shown in black boxes; blue triangles are for the A. Short's results (((A. Short 2006), Fig. 6 on page 15) by Gauss fitting of the CCN10 data; red dots are for data from the S. Brown's Analysis ((S. Brown & F. Van Leeuwen 2008), Fig. 19 on page 27).

Table 1

Parameters of the power law $y = aS^b$ best fitting the charge loss measurements

DoB	*Parameter*	*Value*	*Error*
	a	0.236	0.046
0	b	1,027	0.018
	a	0.023	0.003
5	b	1,235	0.013
	a	0.010	0.001
10	b	1,301	0.008

Table 2

SNR for DoB=0 sessions

STAR	$S = 200$	$S = 400$	$S = 650$	$S = 2,000$	$S = 7,000$	$S = 60,000$
A	7.12	15.33	18.20	35.41	64.29	190.09
B	9.38	18.04	21.07	40.95	73.65	216.73
C	10.50	19.75	23.68	45.16	80.61	237.36
D	11.21	21.16	25.30	47.62	85.54	251.18
E	10.72	20.16	25.54	47.16	85.15	252.77
F	9.31	18.27	24.76	44.35	80.07	236.94
G	8.27	16.10	23.40	40.32	72.52	211.75
H	7.49	15.26	22.74	38.66	69.80	201.38
I	7.00	14.69	21.20	36.75	66.80	191.55
J	6.43	12.60	19.17	33.08	61.04	176.97

Table 3

SNR for DoB=5 sessions

STAR	$S = 200$	$S = 400$	$S = 650$	$S = 2,000$	$S = 7,000$	$S = 60,000$
A	6.10	11.18	15.21	35.56	69.08	214.83
B	7.77	13.72	18.13	41.62	78.69	244.88
C	8.65	17.18	20.74	46.08	86.22	268.66
D	9.49	17.18	22.40	49.36	91.66	284.63
E	9.90	17.39	22.57	50.38	93.29	288.58
F	9.19	17.15	21.81	48.67	90.07	275.83
G	8.70	15.63	20.24	45.87	84.67	253.57
H	8.02	14.90	19.50	44.11	81.65	241.98
I	7.65	13.67	18.00	42.18	78.06	228.87
J	6.86	12.18	16.16	37.48	69.87	210.44

Table 4

SNR for DoB=10 sessions

STAR	$S = 200$	$S = 400$	$S = 650$	$S = 2,000$	$S = 7,000$	$S = 60,000$
A	4.94	12.92	16.84	28.40	64.41	202.35
B	6.27	15.62	19.36	34.21	73.70	230.83
C	6.99	17.06	22.07	38.25	80.86	253.35
D	7.74	18.56	23.69	41.00	85.91	268.54
E	8.11	19.20	24.02	42.30	87.44	272.01
F	7.44	18.82	23.62	41.64	85.13	257.65
G	6.98	18.15	22.88	39.18	79.97	236.50
H	6.47	16.22	21.36	37.33	77.41	226.72
I	6.13	15.74	20.38	35.16	73.91	215.50
J	5.42	13.66	18.03	31.28	67.80	197.33